Virgin and Extracted Soots in Premixed Methane Flames: A Comparison of Surface Functional Groups, Graphitization Degree, and Oxidation Reactivity.

Version: Accepted Version

Article:

Liu, Y orcid.org/0000-0002-9367-3532, Song, C, Lv, G et al. (2 more authors) (2017) Virgin and Extracted Soots in Premixed Methane Flames: A Comparison of Surface Functional Groups, Graphitization Degree, and Oxidation Reactivity. Energy & Fuels, 31 (6). pp. 6413-6421. ISSN 0887-0624

https://doi.org/10.1021/acs.energyfuels.6b03011

Virgin and extracted soots in premixed methane flames: A comparison of surface functional groups, graphitization degree and oxidation reactivity

Ye Liu, Chonglin Song*, Gang Lv, Xiaowei Wang, Na Li

State Key Laboratory of Engines, Tianjin University, Tianjin 300072, China

Abstract: This study reports the similarities and differences in the physicochemical properties of virgin soot generated in premixed methane flames and the corresponding extracted soot following removal of its soluble organic fraction (SOF). In addition, the correlations between these physicochemical properties and the SOF content are investigated. Soot samples were acquired at varying heights above the burner using a probe sampling technique, and surface functional groups (SFGs) and degree of graphitization were analyzed by Fourier transform infrared and Raman scattering spectroscopy. The oxidation reactivities of both the virgin and extracted soots were evaluated in terms of the characteristic oxidation temperatures and apparent activation energies, based on thermogravimetric analysis. Both materials undergo similar changes in the concentrations of aliphatic and aromatic C–H, A_{D1}/A_G and A_{D3}/A_G ratios, and apparent activation energy with increasing height above the burner, but differ in their A_{D4}/A_G ratios. The presence of the SOF does increase the relative concentrations of aliphatic and aromatic C–H groups. Moreover, at the same sampling position, the A_{D1}/A_G, A_{D3}/A_G and A_{D4}/A_G ratios of the virgin soot are greater than those of the extracted soot, while the apparent activation energy values of the virgin soot are lower. These data indicate that the virgin soot possesses less graphitic organization and lower resistance to oxidation relative to the

---

* Corresponding author. Tel.: +86-22-27406840-8020; fax: +86-22-27403750

Email address: songchonglin@tju.edu.cn (C.-L. Song)

extracted soot. In addition, there is a definite correlation between the oxidation reactivity and the SOF content.

Keywords: Premixed flame; Virgin soot; Extracted soot; Surface functional group; Graphitization degree; Oxidation reactivity

1. Introduction

It is known that the soluble organic fraction (SOF) adsorbed on particulate matter (PM) generated by combustion processes results from unburned hydrocarbons.[1,2] Typically, the SOF accounts for 5%–60% of the overall PM mass,[2,3] depending on the fuel composition and combustion conditions. The SOF consists primarily of aliphatic hydrocarbons, polycyclic aromatic hydrocarbons (PAHs), and nitric- or oxi-PAHs,[4] including a large number of aromatic and aliphatic C–H groups. The physicochemical properties of soot particles have been studied extensively, owing to their association with soot formation and oxidation processes.[5–8] As a major component of PM, the SOF exerts a non-negligible effect on the physicochemical properties of soot. Ishiguro et al.[9] discovered that virgin soot possesses higher oxidation reactivity than heat-treated soot, and that diesel soot has a highly porous structure following the release of the SOF occluded within the soot particles. They interpreted these results to mean that the increased specific surface area of soot following release of the SOF facilitates the access of oxygen to pores in the soot, thus enhancing the soot oxidation reactivity. Collura et al.[10] compared the variations of the graphitization degree of diesel soot. They determined that the presence of SOF on soot reduces the graphitic organization, and the thermal decomposition of SOF absorbed on soot leads under inert atmosphere to the formation of a microporous carbonaceous layer. Chong et al.[4] examined the effects of volatile component of SOF on the oxidation of diesel PM. They found that the oxidation characteristics of diesel PM are only weakly influenced by the volatile components of SOF. In contrast, the heavier SOF components and thermal aging seem to have a strong influence on diesel soot oxidation. In the study of Lee et al.,[11] it was revealed that the diesel PM with a higher content of SOF oxidizes more rapidly. However, Ahlström et al.[12] suggested that the SOF adsorbed on diesel soot preferentially vaporizes before the soot reaches its ignition temperature and thus exerts a limited impact on soot reactivity. Up to the present time, many investigations have been carried out related to the combustion-generated soot, but there is no consensus about the effect of SOF on soot oxidation feature. Moreover, the information concerning the effect of SOF on surface functional groups and graphitization degree of soot is still limited.

Motivated by the above considerations, the purpose of the present research was to obtain further insights into the effects of the SOF on the physicochemical properties of soot, including surface functional groups (SFGs), graphitization degree and oxidation reactivity. Due to the complexity of diesel combustion and diesel component, the SOF on diesel soot is more complicated than that on flame-generated soot in compositions. Moreover, the vaporized lubricating oil during the diesel combustion process can make the metallic species deposit on the soot particles[13], and these metallic species appear to be good catalysts in the soot oxidation[13-15]. Thus, the soot generated from a methane premixed flame was employed to investigate the effects of SOF on the SFGs, graphitization degree and oxidation reactivity. A probe sampling technique was employed to obtain soot samples formed at different heights above the burner (HAB). The separation of SOF on these soot samples was performed by means of the Soxhlet extraction technique. The SFGs and graphitization degree of each soot sample were characterized using Fourier transform infrared (FT-IR) and Raman spectroscopy. The characteristic oxidation temperatures and oxidation reactivities of soot samples were assessed by thermogravimetric analysis (TGA). In addition, an attempt was made to determine the correlation between various physicochemical properties and the SOF content.

2. Experimental

2.1. Burner and sampling system

The schematic diagram of the experimental system is as shown in Fig. 1. A laminar premixed flame was produced at atmospheric pressure by employing a 25 mm diameter sintered bronze McKenna burner (Holthuis & Associates, Sebastopol, USA). The burner was mounted on a motorized translation stage with a positional accuracy of 0.01 mm, allowing vertical movement relative to the fixed sampling system. A constant temperature cooling water tank was used to maintain the initial mixture gas temperature at 300 K. The central tube of the burner supplied a mixture of methane (40.65 mol%), air (32.25 mol%) and oxygen (27.1 mol%), while the concentric porous ring was used to generate a N_2 shield (at a flow rate of 30 L/min) that eliminated any effect of the surrounding air on the flame. Three independent mass-flow controllers, each with an accuracy of ±0.02%, controlled the flow of methane, air, oxygen and the shielding gas, respectively. The fuel/air equivalence ratio in the flame was maintained at 2.4 and the velocity of the cold mixture gas was held constant at 4 cm/s.

Soot samples were acquired at various heights (5, 8, 12, 16 and 25 mm) along the axis of the premixed flame using a probe sampling technique.[16,17] A stainless steel probe with a diameter of 3.175 mm and a wall thickness of 0.125 mm was positioned horizontally over the burner, and a sampling orifice with a diameter of 0.15 mm was drilled in the middle of the probe using a laser, facing downward toward the incoming burning gas. This probe, now with a sampling orifice, was connected to a vacuum system with an in-line Teflon filter to collect the PM. We used cold N_2 at a rate of 26.8 L/min (STP) to dilute the sucked flame gas for the purpose of effectively quenching chemical reactions in the sampling line.[18] On the other hand, the use of dilution can make sure to harvest the soot samples at a relatively low temperature. The used dilution ratio of sucked flame gas was determined by means of scanning mobility particle sizer (SMPS) measurements.[17] The calculation method of dilution ratio follows what was proposed by Zhao et al.[17] The particle size distribution functions (PSDFs) for the dilution ratios of the flame gas in the sample probe were shown in Fig. 2. There are significantly different shapes in the PSDF between the dilution ratios of 20 and 300. When further increasing the dilution ratio to 500, however, the PSDFs show a very similar shape to those at the dilution ratio of 300, that is, both of PSDFs are unimodal at low HAB and then change to be bimodal as the HAB increased. Zhao et al.[17] concluded that when a critical dilution ratio is reached, the shape of the PSDFs should become independent of the dilution ratio. In the present work, this similarity in the shape of the PSDF suggests that chemical reactions of soot particles can be prevented at the dilution ratio of 300. Thus, a dilution ratio of 300 was used in our experiment.

The collection time for each trial was varied from 10 to 20 min. Generally, sampling at a lower flame position required much more time than at higher positions. After sampling, the soot samples were scraped from one filter and collected for analysis without any pre-treatment. This material is termed the virgin soot. The same soot samples on the other filter were extracted with dichloromethane using the Soxhlet method.[19] The SOF mass was calculated by the difference in the mass of the filter paper before and after Soxhlet-extracting virgin soot, using an electronic microbalance (Sartorius ME 95 5-F) with an accuracy of 0.001 mg. The virgin soot mass was calculated by the difference in the mass of the filter paper before and after sampling. The ratio of

SOF mass to virgin soot mass is the SOF percentage. The soot was subsequently separated from the Teflon filter by ultrasonication in dichloromethane, followed by centrifugal separation.[20] The resulting soot samples, termed extracted soot, were dried under nitrogen and then sealed in glass bottles while awaiting analysis. The temperature along the axial direction of the flame was measured using an R-type thermocouple (Pt/Pt-13%Rh) with a 30 μm wire and a bead diameter of approximately 150 μm. This device was attached to an electrically powered cylinder (Festo, DNCE-32-320-LAS) that allowed the rapid insertion and withdrawal of the thermocouple so as to reduce the thermocouple exposure time in the flame. The temperature values thus obtained were corrected for radiative heat loss,[21] and the uncertainty in the flame temperature measurements was determined to be no greater than ±50 K.

2.2. Fourier transform infrared spectroscopy (FT-IR)

FT-IR spectroscopy was applied to identify the SFGs and to quantify the relative amounts of aliphatic and aromatic C–H groups on the sample surfaces. FT-IR spectra in the 4000-400 cm^{-1} range were acquired with a Nicolet Nexus 470 FT-IR spectrometer with a resolution of 1 cm^{-1}, using samples prepared by mixing and grinding the soot with KBr at a concentration of 0.5 wt% and pressing into pellets under 10 tons for 5 min. Spectra were baseline-corrected and smoothed prior to analysis and a continuous background was subtracted from each sample spectrum. Three spectra were acquired for each sample to allow an estimation of the reproducibility of the method. In general, the uncertainty in the FT-IR measurements was found to be less than 5%.

2.3. Raman scattering spectroscopy

A Raman scattering spectrometer (Renishaw RM1000) was used to characterize the degree of graphitization of the virgin and extracted soots. Spectra were acquired over the wavelength range from 900–2000 cm^{-1} with an Ar laser excitation source operating at 514.5 nm and 20 mW, and a sample scanning area 2 μm in diameter. Spectra were obtained at approximately 10 positions with an exposure time of 60 s, and average data were calculated with an uncertainty of less 5%. Curve fitting for the Raman spectra was carried out using the Peak Fitting Module in the Origin 9.0 software package.

2.4. Thermogravimetric analysis (TGA)

The virgin and extracted soot reactivities were estimated from the apparent activation energy values obtained by TGA (Mettler-Toledo TGA/DSC1) using platinum crucibles. Experiments were performed in ultra-high purity air at a flow rate of 40 mL/min and samples exposed to this air flow were heated from 50 to 800 °C at 10 °C/min. Each analysis was repeated three times to ensure reproducibility. The apparent activation energies for the virgin and extracted soots were calculated using the Mettler-Toledo STARe software (version 9.20) via the Friedman method, as suggested by Muller et al.[22]

3. Results and discussion

3.1. Surface functional groups

As noted, FT-IR spectroscopy was employed to identify and quantify the SFGs on the soot surface. Fig. 3 shows typical baseline-corrected and smoothed FT-IR spectra of the virgin and extracted soots. Both spectra display weak peaks around 3050 cm^{-1}, corresponding to aromatic C–H stretching. The three well-defined peaks at 770, 840 and 880 cm^{-1} are assigned to the out of plane aromatic hydrogen bending modes of three-adjacent, two-adjacent and isolated hydrogens, respectively.[23] In addition, three characteristic aliphatic C–H stretching peaks are observed at 2960, 2920 and 2860 cm^{-1}. Aliphatic C–H groups are primarily due to methyl, methylene and methine groups bonded to aromatic rings on PAHs, or to methylene bridges (fluorene types) maintaining the interconnection between PAHs within a network.[24,25] Other characteristic peaks are also evident in the region between 1720 and 1280 cm^{-1}. The weaker ones around 1600 cm^{-1} are assigned to C=C aromatic stretching, while the C=O stretching of carboxylic acids appears at 1720 cm^{-1},[24,25] and the aliphatic C–H plane deformations of CH_2/CH_3 groups appears at 1440 and 1380 cm^{-1}.

For the purposes of SFG quantification, the FT-IR spectra were deconvoluted into different Gaussian functions, and the peak positions and band widths obtained from the best fitting Gaussian functions are listed in Table 1. Because quantitation based on peak area is more reliable than that based on peak height,[26] this process was used to quantify the concentration of each SFG. According to Mckinnon et al.,[24] Russo et al.[26] and our previous work,[20] the ratios of the aliphatic C–H peak area at 2920 cm^{-1} and the sum of aromatic C–H peak area at 770, 840 and 880 cm^{-1} to the aromatic C=C peak area at 1600 cm^{-1} (A_{2920}/A_{1600} and A_{aro}/A_{1600}) can be used to determine the relative concentrations of aliphatic and aromatic C–H groups, respectively. This method is unaffected by the thickness and concentration of the KBr pellet. Fig. 4 plots the A_{2920}/A_{1600} and A_{aro}/A_{1600} ratios as functions of the HAB. The A_{2920}/A_{1600} and A_{aro}/A_{1600} values for the virgin soot are evidently larger than those for the extracted soot at each sampling position, especially at low flame positions (below 8 mm), implying that the SOF contains a large number of aliphatic and aromatic C–H groups.

The relative concentrations of aliphatic C–H groups in the virgin and extracted soot samples in Fig. 4a exhibit a decrease as HAB increases, following a sharp increase on going from HAB = 5 to 8 mm, whereas the relative concentrations of aromatic C–H groups plotted in Fig. 4b increase continuously along the axial position of the flame. In the study of premixed *n*-heptane flames performed by Anna et al.,[27] it was found that fuel and oxygen are consumed quickly at low flame positions, and at the same time H_2 is detected and increase steeply. Russo et al.[28] reported that in a premixed methane flame, approximately 70% volume fraction of molecular hydrogen is found in the HAB range of 5-8 mm. The presence of large amounts of molecular hydrogen deactivates soot and soot precursor radicals,[28] which prevents the rapid consumption of aliphatic hydrogen, such that the quantity of aliphatic hydrogen generated by thermal decomposition exceeds the amount consumed. This increase in aliphatic hydrogen is evidenced by the elevation in the A_{2920}/A_{1600} ratio over the HAB range of 5 to 8 mm, as shown in Fig. 4a. However, Cain et al.[16] attributed the increase in aliphatic hydrogen to the reaction of unsaturated hydrocarbons (e.g., acetylene) with the surface of an initially graphitic-like core, leading to bonding of aliphatic compounds on this core to form the aliphatic shell. As the HAB increases further, the persistent decrease in the A_{2920}/A_{1600} ratio suggests that the abundant aliphatic hydrogen on soot surface is gradually consumed. This behavior is likely due to the enhanced carbonization reactions on the soot surface. Dobbins and his colleagues[29-31] studied the chemical evolution of soot precursor particles on the centerline of the laminar ethene diffusion flame. They found that carbonization on the centerline of flame occurs abruptly between 30 and 40 mm above the burner, where the hydrogen mole fraction on soot decreases from 0.36 to 0.15. Vander Wal.[32] claimed that the soot carbonization process in the diffusion flame accounts for the decrease in hydrogen mole fraction. Moreover, the energy required for the abstraction of the first hydrogen of methylene groups is lower than that for methyl groups and much lower than that for aromatic hydrogen.[28] Over the HAB range of 5–8 mm, therefore, methylene groups are readily removed to generate more active sites available for the further formation of aromatic compounds, resulting in a sharp increase in the A_{aro}/A_{1600} ratio. At higher HAB values, the gradual increase in the A_{aro}/A_{1600} ratios occurs because the enhanced carbonization reactions reduce the concentration of available radical sites, decreasing the reactivity required for the additional formation of aromatic compounds. Russo et al.[28] calculated the concentrations of aliphatic and aromatic hydrogen tethered to soot samples by multiplying their hydrogen weight fraction, measured by FT-IR analysis, by soot concentration. As the HAB increases, the aliphatic hydrogen concentration exhibits rise-decay trend along the flame axis, whereas the aromatic hydrogen concentration shows an increase. In contrast, the aliphatic and aromatic hydrogen weight fractions both decrease along the flame axis with an increase in HAB. However, Santamaria et al.[33] reported that the concentration of aromatic groups on soot from an inverse ethylene diffusion flame increases with an increase in the HAB. They concluded that the increased quantities of aromatic compounds can be ascribed to the fact that aliphatic structures undergo de-alkylation and/or cyclization reactions.

3.2. Graphitization degree

The degrees of graphitization of soot samples were characterized by Raman spectroscopy because this technique is sensitive to the fundamental atomic vibrations of the graphite lattice. Fig. 5 shows typical baseline-corrected, smoothed Raman spectra of virgin and extracted soots from the premixed methane flames. These spectra exhibit two board and highly overlapped peaks at approximately 1345 (D peak) and 1590 cm^{-1} (G peak). To allow a more accurate analysis, the spectra were deconvoluted and fitted by three Lorentian and one Gaussian functions,[34] and the obtained results are shown in Fig. 6. The Lorentian functions correspond to the D1 band arising from the carbon atoms at the edge of the graphene layers,[13] the D4 band from the C–C and C=C bonds in polyene-like structures[35,36] and the G band from the ideal graphitic lattice,[34] while the D3 band assigned to the amorphous carbon fraction of the soot[35] corresponds to the Gaussian function. Table 2 lists the fitted data, including full width at half maximum (FWHM) values and peak positions. For both the virgin and extracted soots, the FWHMs of the G bands are narrower than those of the other three bands, demonstrating that the G peak corresponds to the crystalline phase of carbon.

The relative D peak to G peak intensity (I_D/I_G) is directly relates to the size and defects in the basal plane of the graphene layers, i.e., follows the equation: $I_D/I_G = C/L_a$, where C is a constant.[37] But when L_a is smaller than 2 nm, Ferrari et al.[38,39] proposed that such linear relationship between $1/L_a$ and I_D/I_G breaks down. The relationship between I_D/I_G ratio and average crystallite size L_a follows a new equation: $I_D/I_G = C'(\lambda) L_a^2$. In other words, the increase in I_D/I_G ratio indicates an increase in graphitization degree of soot. However, some research results cannot be explained with the equation suggested by Ferrari et al. For instance, Vander Wal et al.[40,41] discovered that in the case of $L_a < 2$ nm, the soot structure becomes more graphitic with the decrease in I_D/I_G ratio. Rohani et al.[42] found that the diesel exhaust soot obtained from the conventional combustion mode had lower I_{D1}/I_G and A_{D1}/A_G than those from premixed charge compression ignition (PCCI) combustion mode. They claimed that the conventional mode soot possesses more graphitic organization than the PCCI mode soot. Seong and Boehman[13] asserted that the equation proposed by Ferrari et al. is not applicable for soot samples because soot samples are different from carbon materials. Because the FWHM cannot be reflected in the peak intensity ratio[34,43] and the D and G peaks of Raman spectrum are the cumulative results of D1, D3, D4 and G peaks[42], the peak area ratio (A_{D1}/A_G) was used to characterize the graphitization degree of soot in the present study. The decrease in A_{D1}/A_G ratio indicates an increase in graphitization degree of soot. The peak area ratios of A_{D1}/A_G, A_{D3}/A_G and A_{D4}/A_G against the HAB are plotted in Fig. 7. The A_{D1}/A_G and A_{D3}/A_G ratios of the virgin soot are greater than those of the extracted soot at each sampling position, implying that the virgin soot possesses a more disordered, amorphous structure compared to the extracted soot. This is believed to result from the presence of an appreciable amount of amorphous soot precursors in the SOF[13,44]. In contrast, the higher A_{D4}/A_G values for the virgin soot indicate that there are high concentrations of C–C and C=C bonds related to polyene-like structures in the SOF.[36,45] Collura et al.[10] found the diesel exhaust soot exhibited relatively ordered graphitic organization after thermal decomposition process of SOF. Especially, when using an oxidation catalyst on the diesel engine, the soot after thermal decomposition becomes even more ordered graphitic organization than the virgin soot. Moreover, both the virgin and extracted soots exhibit similar trends in terms of changes in the A_{D1}/A_G and A_{D3}/A_G ratios as the HAB increases. In the region of HAB $<$ 8 mm, there are dramatic increases in the A_{D1}/A_G and A_{D3}/A_G ratios for both the virgin and extracted soots, suggesting a decrease in the graphitization degree of the soot. Over the HAB range of 12 to 25 mm, increased rates of carbonization reactions and longer residence time enhance the degree of graphitization, and consequently decrease the A_{D1}/A_G and A_{D3}/A_G ratios. Russo et al.[46] reported that methane soot undergoes a progressive dehydrogenation process with the increase in the residence time, which leads to an increase in the degree of graphitization. Dobbins et al.[29-31] discovered that carbonization reaction occurs abruptly at relative high flame positions, accompanying with the significant consumption of hydrogen mole fraction and the improved degree of graphitization. The A_{D4}/A_G value steadily decreases in the case of the virgin soot as the HAB increases, while the extracted soot shows a decrease after an initial increase. At low flame positions, the difference in the variations of the A_{D4}/A_G ratios between both soots is likely due to the presence of species with C–C and C=C bonds of the polyene-like structures in the SOF of virgin soot, which play an important role in the soot growth process.[36,45]

3.3. Characteristic oxidation temperatures and reactivity

3.3.1. Peak and burnout temperatures

Figure 8 presents a typical smoothed TGA-differential thermal gravimetry (DTG) plot (showing differential mass loss) generated by the virgin and extracted soots. Two characteristic temperatures were obtained from these DTG curves:[5,47] the peak temperature (T_{p}) and the burnout temperature (T_{b}). T_{p} refers to the temperature at which the maximum rate of weight loss occurs, and a lower T_{p} suggests easier ignition. T_{b} represents the temperature at which the oxidation of soot is complete. The T_{p} and T_{b} values for both the virgin and extracted soots are presented in Table 3. Over the range of experimental flame positions, the T_{p} and T_{b} values for the virgin soot are shifted to lower temperatures by 5–27°C relative to the data for the extracted soot. These results indicate that the virgin soot ignites more easily and that its combustion is completed sooner than that of the extracted soot. That is, the oxidation reactivity of the virgin soot is increased because of the presence of the SOF. Similar results were reported by Yehliu et al.[48,49] and Xu et al.,[50] who found that the presence of SOF on soot increases the oxidation reactivity. For the virgin soot, considerable SOF resides inside the micropores or between the primary particles. During the heating process, the SOF is preferential evaporated. Although the SOF does not participate in the soot oxidation process, larger porous surface is exposed into the oxidation environment, which propagates more surface available for oxidation reaction.[51,52]

3.3.2. Oxidation reactivity

The oxidation reactivity of flame-formed soot is evaluated in terms of the apparent activation energy (E_a). The calculation of the apparent reactivation energy is based on the Arrhenius equation:

$$-\frac{dm}{dt} = k \cdot m^n = Ae^{-\frac{Ea}{RT}} m^n \, , \tag{1}$$

where m is the actual mass of the sample undergoing reaction, t is the reaction time, k is the specific rate constant, T is the absolute temperature of the sample, A and E_a are the Arrhenius pre-exponential factor and apparent activation energy, respectively, and n is the reaction order. It was assumed that $n = 1$ during sample oxidation in this work.[5]

E_a values were calculated from the slopes of plots of $\ln(-\frac{dm}{dt}\frac{1}{m})$ against $1/T$ and are plotted as functions of the HAB in Fig. 9. The E_a values of the extracted soot are in the range of 132.25 to 153.20 kJ mol^{-1}, and these values are greater than those of 124.22 to 151.38 kJ mol^{-1} for the virgin soot, implying that the virgin soot is more readily oxidized. This observation can be explained by the difference in the specific surface areas of these materials. During the ongoing oxidation, the SOF on the virgin soot surface will evaporate and/or decompose, which increases the specific surface area.[9,10] The resulting greater specific surface area exposes more edge active positions to oxygen attack.[53] Chong et al.[4] examined the effects of volatile component of SOF on the oxidation of diesel exhaust PM collected directly from the filter membrane of a DPF. They found that the oxidation characteristics of diesel PM were weakly influenced by the volatile components of SOF. In contrast, the heavier SOF components and thermal aging seemed to have a strong effect on diesel soot oxidation. Lee et al.[11] analyzed the oxidation properties of the diesel PM from the high-temperature exhaust stream of a single-cylinder direct-injection diesel engine. They pointed out that the PM with a higher content of SOF was oxidized more rapidly. Moreover, both the virgin and extracted soots exhibit similar trends in terms of changes in E_a with increasing HAB values. The oxidation reactivity of soot is related to the amounts of SFGs and the degree of graphitization, and a high concentration of SFGs and a low degree of graphitization can improve the reactivity.[20,54] Over the range of HAB values from 5 to 8 mm, the decreased E_a values of the virgin and extracted soots are attributed to greater amounts of SFGs and more amorphous structures. As the HAB increases further, from 8 to 25 mm, the increase in E_a for both soots can be ascribed to the evolution of a more graphitic nanostructure and the presence of fewer aliphatic and aromatic C–H groups, as demonstrated in Figs. 4 and 7.

3.4. Relationship between physicochemical properties and SOF content

To establish a possible correlation between the physicochemical properties and the SOF content, the A_{2920}/A_{1600}, $A_{\mathrm{aro}}/A_{1600}$ and $A_{\mathrm{D1}}/A_{\mathrm{G}}$ ratios and E_a values of the virgin soot were normalized with respect to those of the extracted soot. The normalized values for the soot samples at different HAB values are plotted against the SOF content in Fig. 10. It is evident that, as the SOF content increases, the normalized concentrations of aliphatic and aromatic C–H and $A_{\mathrm{D1}}/A_{\mathrm{G}}$ ratios increase, whereas the normalized E_a values decrease. To assess the strength of the linear relationship between these variables, the linear correlation coefficient, R^2, was calculated by means of simple linear regression. The R^2 values are 0.01 between the normalized concentrations of aliphatic groups and the SOF content, 0.33 between the normalized concentrations of aromatic C–H groups and the SOF content, and 0.18 between the normalized $A_{\mathrm{D1}}/A_{\mathrm{G}}$ ratio and the SOF content. While a value of 0.97 was found for the relationship between the normalized E_a and the SOF content. These results suggest that the SOF content has a limited correlation with the concentrations of aliphatic and aromatic C–H and graphitization degree, but has a definite correlation with the normalized E_a. Therefore, the SOF content can serve as an indicator of the oxidation reactivity of soot. This result is in accordance with the findings of Stratakis et al.,[55] who reported that an increase in the SOF content coincides with a decrease in E_a. Collura et al.[10] also observed that larger amounts of SOF are associated with higher oxidation reactivity. Lee et al.[11] also reported that soot having higher SOF fraction oxidizes more rapidly relative to those with lower SOF fraction.

4. Conclusions

A comparative study of the physicochemical properties of virgin and extracted soots was carried out, employing a premixed methane flame. Compared with the extracted soot, the virgin soot shows relatively high concentrations of aliphatic and aromatic C–H groups, larger A_{D1}/A_G, A_{D3}/A_G and A_{D4}/A_G ratios, as well as smaller Ea values at all axial flame positions. Moreover, T_p and T_b of the virgin soot are shifted to lower temperatures by 5–27 °C compared with those of the extracted soot, suggesting that the virgin soot should ignite more readily at a lower temperature and its combustion should be complete sooner. However, the variations in the amounts of aliphatic and aromatic C–H groups, the A_{D1}/A_G and A_{D3}/A_G ratios, and the Ea values for the virgin soot are similar to those for the extracted soot throughout the flame. The exception is in the case of the A_{D4}/A_G ratio. In both the virgin and extracted soots, the relative amounts of aliphatic C–H groups increase over the range of HAB values from 5 to 8 mm and then decrease as the HAB is further increased, while the relative amounts of aromatic C–H groups increase continuously as the HAB increases. The A_{D1}/A_G and A_{D3}/A_G ratios for both virgin and extracted soots were observed to initially increase, then to decrease throughout the axial sampling positions. In contrast, the E_a values for both soots increase at HAB values over 8 mm after a sharp decrease in the lower HAB positions. Finally, the SOF content was found to exhibit a clear correlation with the normalized Ea, while no such correlation was identified with the normalized A_{2920}/A_{1600}, A_{aro}/A_{1600} and A_{D1}/A_G ratios.

Acknowledgments

This study was supported by the National Natural Science Foundation of China (No. 51476115), the National Key Basic Research and Development Program (2013CB228502) and the Tianjin

Research Program of Application Foundation and Advanced Technology (13JCZDJC35800).

References

(1) Durán, A.; de Lucas, A.; Carmona, M.; Ramos, M. J.; Armas, O. Accuracy of the European standard method to measure the amount of DPM emitted to the atmosphere. *Fuel* **2002**, *81* (16), 2053–2060.

(2) Al-Qurashi, K.; Zhang, Y.; Boehman, A. L. Impact of Intake CO2 Addition and Exhaust Gas Recirculation on NOx Emissions and Soot Reactivity in a Common Rail Diesel Engine. *Energy Fuels* **2012**, *26* (10), 6098–6105.

(3) Stanmore, B. R.; Brilhac, J. F.; Gilot, P. The oxidation of soot: a review of experiments, mechanisms and models. *Carbon* **2001**, *39* (15), 2247–2268.

(4) Chong, H. S.; Aggarwal, S. K.; Lee, K. O.; Yang, S. Y.; Seong, H. Experimental investigation on the oxidation characteristics of diesel particulates relevant to DPF regeneration. *Combust. Sci. Technol.* **2013**, *185* (1), 95–121.

(5) Zhang, D. K.; Ma, Y.; Zhu, M. M. Nanostructure and oxidative properties of soot from a compression ignition engine: The effect of a homogeneous combustion catalyst. *Proc. Combust. Inst.* **2013**, *4* (1), 1869–1876.

(6) Ma, Z. H.; Li, L.; Chao, Y.; Kang, N.; Xu, B.; Wu, J. Effects of Diesel Oxidation Catalyst on Nanostructure and Reactivity of Diesel Soot. *Energy Fuels* **2014**, *28* (7), 4376–4382.

(7) Vander Wal, R. L.; Tomasek, A. J. Soot nanostructure: dependence upon synthesis conditions. *Combust. Flame* **2004**, *136* (1), 129–140.

(8) Abián, M.; Jensen, A. D.; Glarborg, P.; Alzueta, M. U. Soot reactivity in conventional combustion and oxy-fuel combustion environments. *Energy Fuels* **2012**, *26* (8), 5337–5344.

(9) Ishiguro, T.; Suzuki, N.; Fujitani, Y.; Morimoto, H. Microstructural changes of diesel soot during oxidation. *Combust. Flame* **1991**, *85* (1-2), 1–6.

(10) Collura, S.; Chaoui, N.; Azambre, B.; Finqueneisel, G.; Heintz, O.; Krzton, A.; Weber, J. V. Influence of the soluble organic fraction on the thermal behaviour, texture and surface chemistry of diesel exhaust soot. *Carbon*

2005, *43* (3), 605–613.

(11) Lee, K. O.; Cole, R.; Sekar, R.; Choi, M. Y.; Kang, J. S.; Bae, C. S.; Shin, H. D. Morphological investigation of the microstructure, dimensions, and fractal geometry of diesel particulates. *Proc. Combust. Inst.* **2002**, *29* (1), 647–653.

(12) Ahlström, A. F.; Odenbrand, C. I. Combustion characteristics of soot deposits from diesel engines. *Carbon* **1989**, *27* (3), 475–483.

(13) Seong, H. J.; Boehman, A. L. Impact of intake oxygen enrichment on oxidative reactivity and properties of diesel soot. *Energy Fuels* **2011**, *25* (2), 602–616.

(14) Song, J.; Wang, J.; Boehman, A. L. The role of fuel-borne catalyst in diesel particulate oxidation behavior. *Combust. Flame* **2006**, *146* (1), 73–84.

(15) Castoldi, L.; Matarrese, R.; Lietti, L.; Forzatti, P. Intrinsic reactivity of alkaline and alkaline-earth metal oxide catalysts for oxidation of soot. *Appl. Catal. B-Environ.* **2009**, *90*(1), 278–285.

(16) Cain, J. P.; Gassman, P. L.; Wang, H.; Laskin, A. Micro-FTIR study of soot chemical composition–evidence of aliphatic hydrocarbons on nascent soot surfaces. *Phys. Chem. Chem. Phys.* **2010**, *12* (20), 5206–5218.

(17) Zhao, B.; Yang, Z. W.; Wang, J. J.; Johnston, M. V.; Wang, H. Analysis of soot nanoparticles in a laminar premixed ethylene flame by scanning mobility particle sizer. *Aerosol Sci. Tech.* **2003**, *37* (8), 611–620.

(18) Tang, Q. X.; Mei, J. Y.; You, X. Q. Effects of CO2 addition on the evolution of particle size distribution functions in premixed ethylene flame. *Combust. Flame* **2016**, *165*, 424–432.

(19) Wang, X. W.; Song, C. L.; Lv, G.; Song, J. O.; Li, H.; Li, B. Evolution of in-cylinder polycyclic aromatic hydrocarbons in a diesel engine fueled with n-heptane and n-heptane/toluene. *Fuel* **2015**, *158*, 322–329.

(20) Wang, L.; Song, C. L.; Song, J. O.; Lv, G.; Pang, H. T.; Zhang, W. Aliphatic C–H and oxygenated surface functional groups of diesel in-cylinder soot: Characterizations and impact on soot oxidation behavior. *Proc.*

Combust. Inst. **2013**, *34* (2), 3099–3106.

(21) McEnally, C. S.; Köylü, Ü. Ö.; Pfefferle, L. D.; Rosner, D. E. Soot volume fraction and temperature measurements in laminar nonpremixed flames using thermocouples. *Combust. Flame* **1997**, *109* (4), 701–720.

(22) Müller, J. O.; Su, D. S.; Jentoft, R. E.; Kröhnert, J.; Jentoft, F. C.; Schlögl, R. Morphology-controlled reactivity of carbonaceous materials towards oxidation. *Catal. Today* **2005**, *102*, 259–265.

(23) Santamaría, A.; Mondragón, F.; Molina, A.; Marsh, N. D.; Eddings, E. G.; Sarofim, A. F. FT-IR and 1 H NMR characterization of the products of an ethylene inverse diffusion flame. *Combust. Flame* **2006**, *146* (1), 52–62.

(24) Mckinnon, J. T.; Meyer, E.; Howard, J. B. Infrared analysis of flame-generated PAH samples. *Combust. Flame* **1996**, *105* (1-2), 161–166.

(25) Santamaría, A.; Mondragón, F.; Quinonez, W.; Eddings, E. G.; Sarofim, A. F. Average structural analysis of the extractable material of young soot gathered in an ethylene inverse diffusion flame. *Fuel* **2007**, *86* (12), 1908–1917.

(26) Russo, C.; Stanzione, F.; Tregrossi, A.; Ciajolo, A. Infrared spectroscopy of some carbon-based materials relevant in combustion: Qualitative and quantitative analysis of hydrogen. *Carbon* **2014**, *74*, 127–138.

(27) D'Anna, A.; Alfe, M.; Apicella, B.; Tregrossi, A.; Ciajolo, A. Effect of fuel/air ratio and aromaticity on sooting behavior of premixed heptane flames. *Energy Fuel* **2007**, *21* (5), 2655–2662.

(28) Russo, C.; Tregrossi, A.; Ciajolo, A. Dehydrogenation and growth of soot in premixed flames. *Proc. Combust. Inst.* **2015**, *35* (2), 1803–1809.

(29) Dobbins, R. A.; Fletcher, R. A.; and Lu, W.; Laser microprobe analysis of soot precursor particles and carbonaceous soot. *Combust. Flame* **1995, ***100* (1), 301–309.

(30) Dobbins, R. A.; Fletcher, R. A.; Chang, H. C. The evolution of soot precursor particles in a diffusion flame. *Combust. Flame* **1998,** *115* (3), 285–298.

(31) Dobbins, R. A.; Govatzidakis, G. J.; Lu, W.; Schwartzman, A. F.; Fletcher, R. A. Carbonization rate of soot precursor particles. *Combust. Sci. Techno.* **1996,** *121*(1-6), 103–121.

(32) Vander Wal, R. L. Soot precursor carbonization: Visualization using LIF and LII and comparison using bright and dark field TEM. *Combust. Flame* **1998**, *112* (4), 607–616.

(33) Santamaría, A.; Yang, N.; Eddings, E.; Mondragon, F. Chemical and morphological characterization of soot and soot precursors generated in an inverse diffusion flame with aromatic and aliphatic fuels. *Combust. Flame* **2010**, *157* (1), 33–42.

(34) Seong, H. J.; Boehman, A. L. Evaluation of Raman parameters using visible Raman microscopy for soot oxidative reactivity. *Energy Fuels* **2013**, *27* (3), 1613–1624.

(35) Cuesta, A.; Dhamelincourt, P.; Laureyns, J.; Martinez-Alonso, A.; Tascón, J. D. Raman microprobe studies on carbon materials. *Carbon* **1994**, *32* (8), 1523–1532.

(36) Dippel, B.; Jander, H.; Heintzenberg, J. NIR FT Raman spectroscopic study of flame soot. *Phys. Chem. Chem. Phys.* **1999**, *1* (20), 4707–4712.

(37) Tuinstra, F.; Koenig, J. L. Raman spectrum of graphite. *J. Chem. Phys.* **1970**, *53* (3), 1126–1130.

(38) Ferrari, A. C.; Robertson, J. Interpretation of Raman spectra of disordered and amorphous carbon. *Phys. Rev. B* **2000**, *61* (20), 14095–14107.

(39) Ferrari A. C.; Basko D. M. Raman spectroscopy as a versatile tool for studying the properties of graphene. *Nat. Nanotechnol.* **2013**, 8, 235–246.

(40) Vander Wal, R. L.; Tomasek, A. J.; Street, K.; Hull, D. R.; Thompson, W. K. Carbon nanostructure examined by lattice fringe analysis of high-resolution transmission electron microscopy images. *Appl. Spectrosc*. **2004**, *58*, 230–237.

(41) Yehliu, K.; Vander Wal, R. L.; Boehman, A. L. A comparison of soot nanostructure obtained using two high resolution transmission electron microscopy image analysis algorithms. *Carbon* **2011**, *49* (13), 4256–4268.

(42) Rohani, B.; Park, S. S.; Bae, C. Effect of injection strategy on smoothness, emissions and soot characteristics of PCCI-conventional diesel mode transition. *Appl. Therm. Eng.* **2016**, *93*, 1033–1042.

(43) Lapuerta, M.; Oliva, F.; Agudelo, J. R.; Boehman, A. L. Effect of fuel on the soot nanostructure and consequences on loading and regeneration of diesel particulate filters. *Combust. Flame* **2012**, *159* (2), 844–853.

(44) Burg, P.; Cagniant, D. Study of the influence of the soluble organic fraction of an exhaust diesel soot by a linear solvation energy relationship approach. *Carbon* **2003**, *41* (5), 1031–1035.

(45) Dippel, B.; Heintzenberg, J. Soot characterization in atmospheric particles from different sources by NIR FT Raman spectroscopy. *J. Aerosol Sci.* **1999**, *30*, 907–908.

(46) Russo, C.; Alfè, M.; Rouzaud, J. N.; Stanzione, F.; Tregrossi, A.; Ciajolo, A. Probing structures of soot formed in premixed flames of methane, ethylene and benzene. *Proc. Combust. Inst.* **2013**, *34* (1), 1885–1892.

(47) Yorulmaz, S. Y.; Atimtay, A. T. Investigation of combustion kinetics of treated and untreated waste wood samples with thermogravimetric analysis. *Fuel Process. Technol.* **2009**, *90* (7), 939–946.

(48) Yehliu, K.; Vander Wal, R. L.; Armas, O.; Boehman, A. L. Impact of fuel formulation on the nanostructure and reactivity of diesel soot. *Combust. Flame* **2012**, *159* (12), 3597–3606.

(49) Yehliu, K.; Armas, O.; Vander Wal, R. L.; Boehman, A. L. Impact of engine operating modes and combustion phasing on the reactivity of diesel soot. *Combust. Flame* **2013**, *160* (3), 682–691.

(50) Xu, Z.; Li, X.; Guan, C.; Huang, Z. Effects of injection pressure on diesel engine particle physico-chemical

properties. *Aerosol Sci. Tech.* **2014**, *48* (2), 128–138.

(51) Leidenberger, U.; Mühlbauer, W.; Lorenz, S.; Lehmann, S.; Brüggemann, D. Experimental studies on the influence of diesel engine operating parameters on properties of emitted soot particles. *Combust. Sci. Technol.* **2012**, *184* (1), 1–15.

(52) Gaddam, C. K.; Vander Wal, R. L. Physical and chemical characterization of SIDI engine particulates. *Combust. Flame* **2013,** *160* (11), 2517–2528.

(53) Vander Wal, R. L.; Mueller, C. J. Initial investigation of effects of fuel oxygenation on nanostructure of soot from a direct-injection diesel engine. *Energy Fuels* **2006**, *20* (6), 2364–2369.

(54) Al-Qurashi, K.; Boehman, A. L. Impact of exhaust gas recirculation (EGR) on the oxidative reactivity of diesel engine soot. *Combust. Flame* **2008**, *155* (4), 675–695.

(55) Stratakis, G. A.; Stamatelos, A. M. Thermogravimetric analysis of soot emitted by a modern diesel engine run on catalyst-doped fuel. *Combust. Flame* **2003**, *132* (1), 157–169.

Figure Captions:

Fig. 1. Schematic diagram of the experimental system.

Fig. 2. Normalized particle size distribution functions (PSDFs) obtained at various dilution ratios.

Fig. 3. Typical infrared spectra of virgin and extracted soots (HAB = 8 mm).

Fig. 4. Relative concentrations of aliphatic and aromatic C–H groups as functions of HAB for virgin and extracted soots. The error bars represent the standard error.

Fig. 5. Typical Raman spectra of virgin and extracted soots (HAB = 8 mm).

Fig. 6. Four-band fitting of typical Raman spectra of extracted soot (HAB = 8 mm).

Fig. 7. A_{D1}/A_G, A_{D3}/A_G and A_{D4}/A_G ratios as functions of HAB. The error bars indicate the standard

error.

Fig. 8. Typical TG-DTG plots for the virgin soot (HAB = 8 mm).

Fig. 9. Apparent activation energy (*Ea*) values as functions of HAB. The error bars indicate the standard error.

Fig. 10. Normalized concentrations of aliphatic and aromatic C–H, A_{D1}/A_G and apparent activation energy (E_a) values as functions of the soluble organic fraction (SOF) content. The error bars indicate the standard error.

Table 1 Data obtained from the curve fitting of the FT-IR spectrum.

	Aliphatic C–H			Aromatic C–H				C=O	C=C
Peak Positions (cm^{-1})	2857±5	2921±4	2958±4	3047±5	778±6	823±6	890±8	1710±8	1600±9
FWHM (cm^{-1})	56±6	46±3	28±2	48±3	24±4	23±2	25±4	55±6	40±6

Table 2 Data obtained from the curve fitting of the Raman spectrum.

	Virgin soot				Extracted soot			
	D4	D1	D3	G	D4	D1	D3	G
Fitting Function	Lorenz	Lorenz	Gaussian	Lorenz	Lorenz	Lorenz	Gaussian	Lorenz
Peak Position (cm^{-1})	1209±7	1341±2	1518±8	1595±5	1190±6	1340±3	1500±9	1587±5
FWHM (cm^{-1})	160±12	150±13	210±8	70±6	120±10	210±12	100±7	80±5

Table 3 Peak and burnout temperatures of the virgin and extracted soots.

HAB	Virgin soot		Extracted soot	
(mm)	T_p (°C)	T_b (°C)	T_p (°C)	T_b (°C)
5	589	637	615	643
8	578	632	605	639
12	594	644	617	652
16	602	660	623	665
25	611	667	635	672

T_p: peak temperature from DTG curve of soot sample oxidation

T_b: burnout temperature from DTG curve of soot sample oxidation

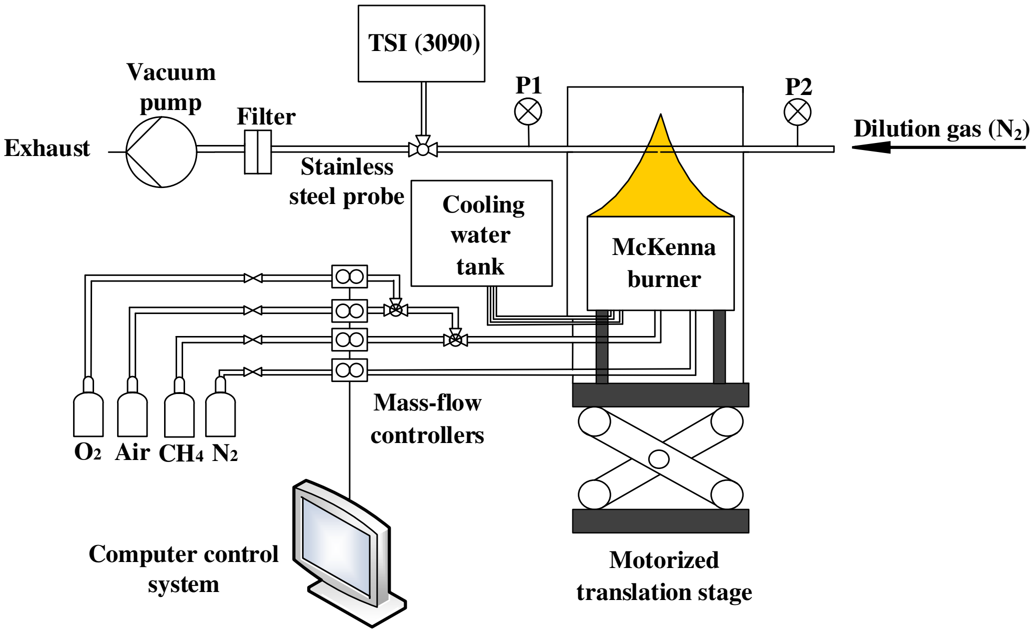

Fig. 1. Schematic diagram of the experimental system.

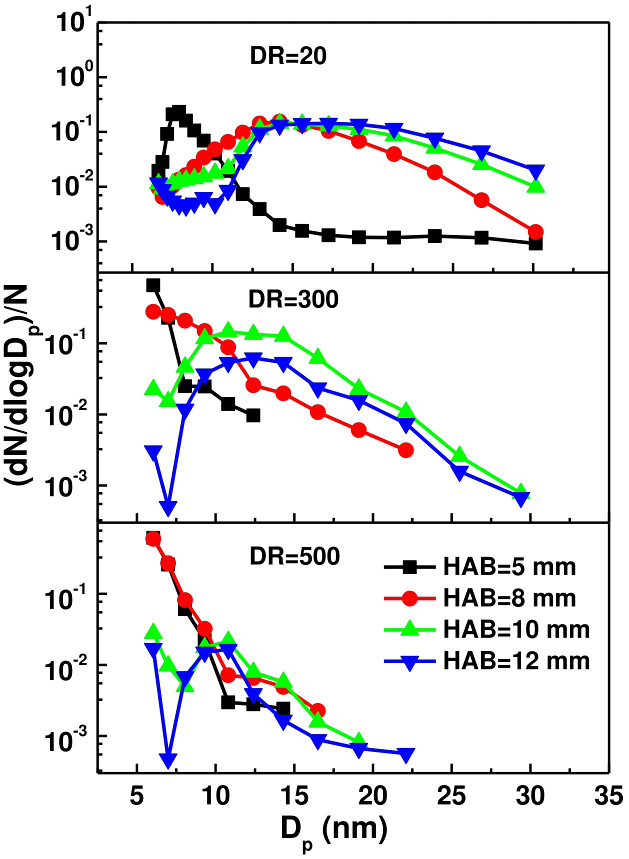

Fig. 2. Normalized particle size distribution functions obtained at various dilution ratios.

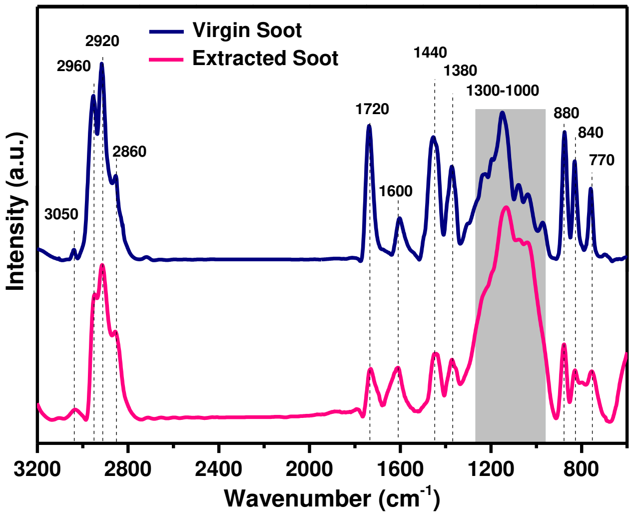

Fig. 3. Typical infrared spectra of virgin and extracted soots (HAB = 8 mm).

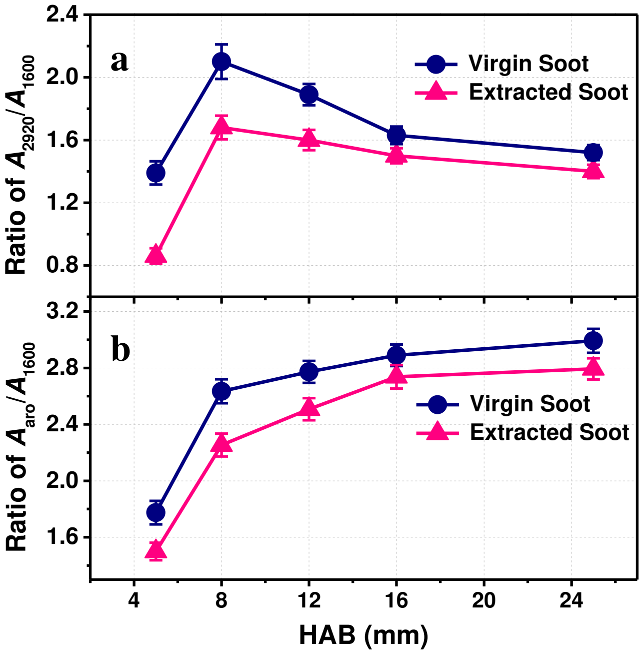

Fig. 4. Relative concentrations of aliphatic and aromatic C–H groups as functions of HAB for virgin and extracted soots. The error bars represent the standard error.

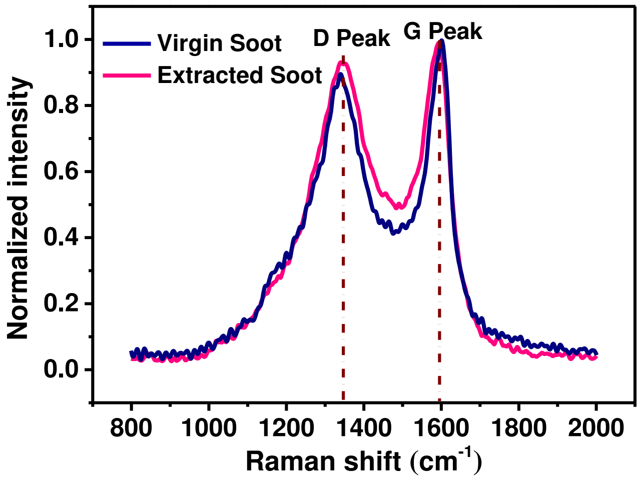

Fig. 5. Typical Raman spectra of virgin and extracted soots (HAB = 8 mm).

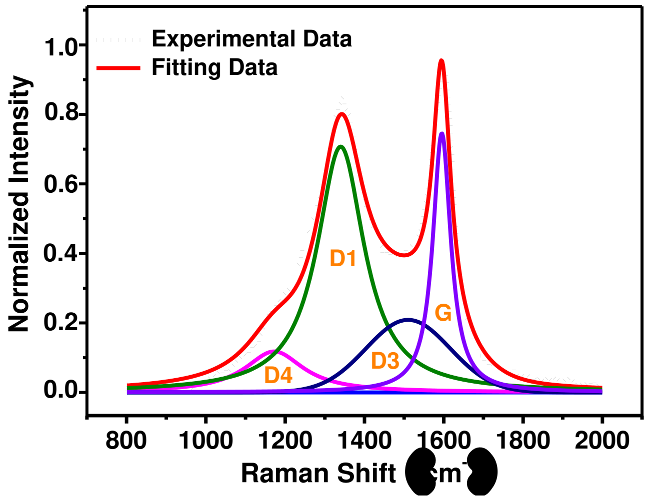

Fig. 6. Four-band fitting of typical Raman spectra of extracted soot (HAB = 8 mm).

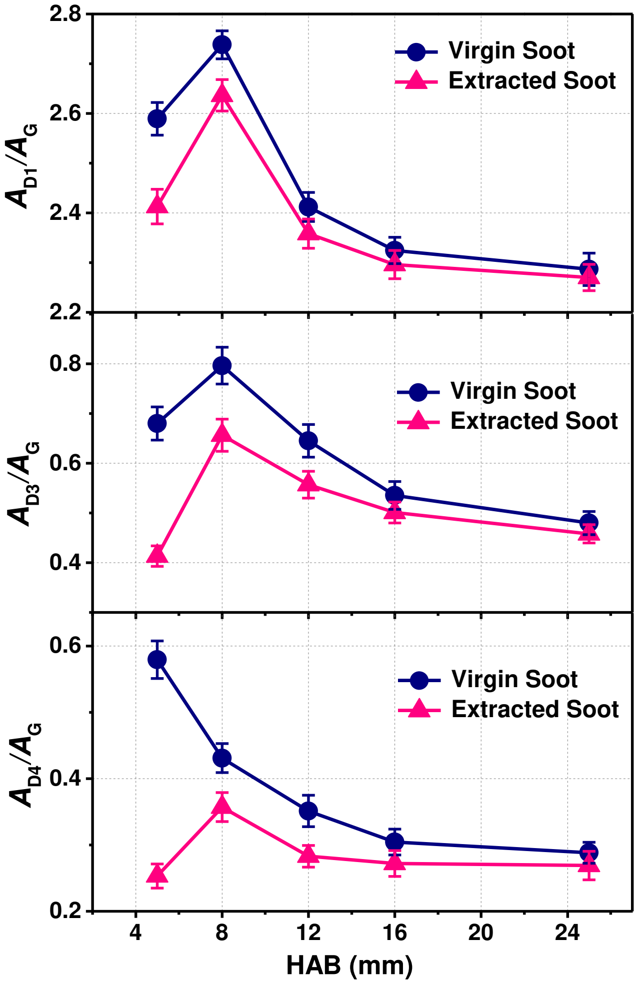

Fig. 7. A_{D1}/A_G, A_{D3}/A_G and A_{D4}/A_G ratios as functions of HAB. The error bars indicate the standard error.

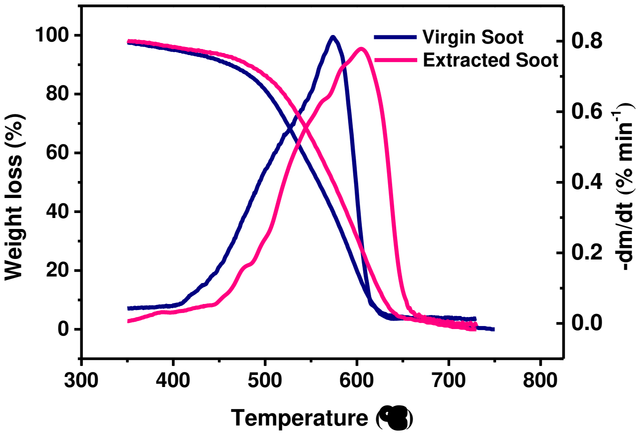

Fig. 8. Typical TG-DTG plots for the virgin and extracted soots (HAB = 8 mm).

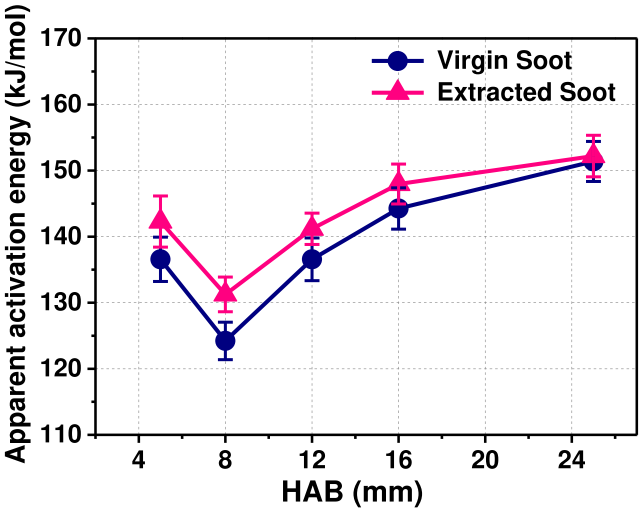

Fig. 9. Apparent activation energy (Ea) values as functions of HAB. The error bars indicate the standard error.

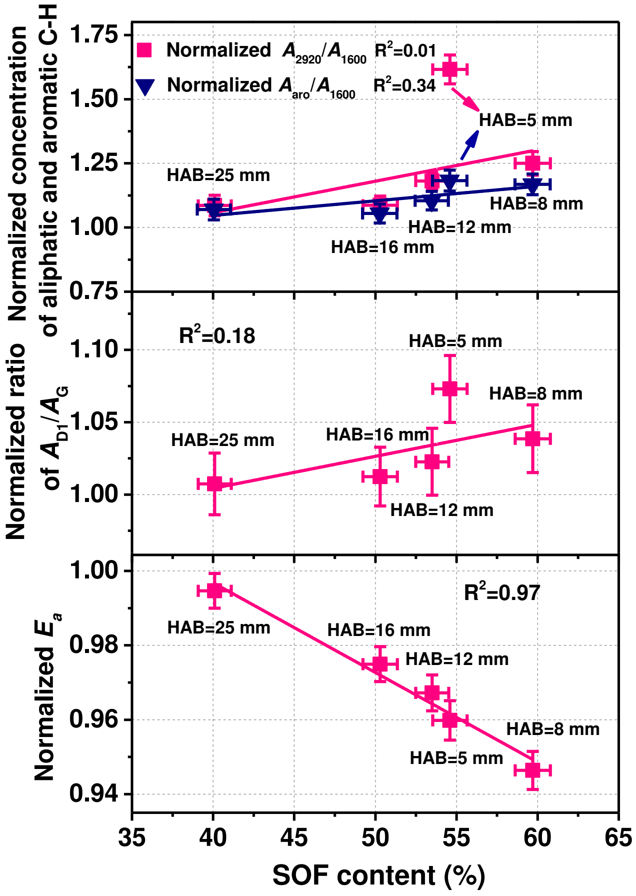

Fig. 10. Normalized concentrations of aliphatic and aromatic C–H, A_{D1}/A_G and apparent activation energy (E_a) values as functions of the soluble organic fraction (SOF) content. The error bars indicate the standard error.